Research Article

Yan-Shuang Yang*, Si-Pei Cheng, Zhan-Rong Zhang, Meng-Yu Yin, and Jia-Wen Hou

Study on the stress field concentration at the tip of elliptical cracks

https://doi.org/10.1515/rams-2022-0259
received May 05, 2022; accepted July 26, 2022

Abstract: The holes and defects in rock materials have a great impact on the mechanical properties and failure mechanism of rock, cracks often appear in the form of flat ellipses in natural rock mass, and the current research is still insufficient. For this purpose, based on the Particle Flow Code (PFC) of discrete element particle flow program, the numerical prefabricated fractured rock samples with the ratios of the long and short axes of the elliptical fractures being 5, 7.5, 10, 12.5, and 15 were simulated in order to obtain the strength and failure characteristics, stress concentration characteristics at tips of numerical rock samples in uniaxial compression test. The results of the numerical test simulation show that: (1) When the rock models with prefabricated elliptical crack were damaged, the initial cracks occurred at the end of the short axis of the elliptical crack, and penetrated up and down from the surface of the elliptical crack, the wing cracks occurred at both ends of the long axis, gradually formed a macro-crack, and the secondary cracks extended near the wing crack. (2) With the increase of the ratios a:b of long and short axes of the elliptical fracture, the strength and elastic modulus of the numerical rock samples gradually decreased, Poisson's ratio gradually increased, and the total number of micro-cracks in the rock models decreased. (3) The numerical solutions of stress concentration factor k obtained by numerical simulations at the tip of the elliptical crack increased with the increase in the ratio of a:b; it was highly consistent with the variation law of the analytical solution of the stress concentration factor calculated by the theory of flat ellipse. The stress concentration is an important reason for failure of rock with elliptical cracks. Study on the crack tip will be very useful and significant.

Keywords: discrete element, precast crack, stress concentration factor, analytical solution

1 Introduction

Micro-cracks and holes in the rock mass are important to the crack propagation, macro-mechanical properties, and failure mechanism of rock. In the aspect of laboratory test, Wang et al. [1] used acoustic emission and digital image correlation to study the spatiotemporal evolution characteristics of crack extension of soft and hard composite laminated rock masses containing double fissures under uniaxial compression. Wu et al. [2] deeply studied the fracture law of rock with cavities, and theoretically studied the rock damage evolution mechanism. Li et al. [3] studied the deformation characteristics of marble with different shapes of holes under uniaxial compression. The research shows that the mechanical properties and failure process of rock were significantly affected by the prefabricated cracks of different geometrical shapes (such as crack angle, crack length, etc.). Chen et al. [4] discussed the influences of the ratio of the long and short axes of the elliptical crack model and the dip angle on the stress distribution area of the rock and the fracture mechanism of the rock sample. In aspect of theoretical research on materials with elliptical cracks, Inglis analyzed the stress of an elliptical void in a flat plate under uniform stress in 1913 [5]. Based on this, Griffith [6] obtained the propagation mechanism of crack tip from perspective of energy, and this theory is still used today.

Due to the difficulties of preparing rock samples with special cracks and the large discreteness of natural rock samples as shown in the laboratory test, numerical modeling techniques for rock with cracks have been widely used in rock engineering [7–11].

In recent years, the numerical simulation program PFC has been favored by many researchers. The numerical samples with parameters obtained from the laboratory test

* **Corresponding author: Yan-Shuang Yang,** School of Civil Engineering, Architecture and Environment, Hubei University of Technology, Wuhan 430068, China, e-mail: y1y1s1@qq.com
Si-Pei Cheng, Meng-Yu Yin, Jia-Wen Hou: School of Civil Engineering, Architecture and Environment, Hubei University of Technology, Wuhan 430068, China
Zhan-Rong Zhang: China Railway Siyuan Survey and Design Group Co., Ltd., Wuhan, Hubei 430063, China

results established in PFC can simulate the interactions of every particle with finite size and number based on the discrete element method (DEM) [12]. For rock samples with special cracks, a numerical model can be easily established in PFC, and the loading process can be simulated based on the results obtained in the laboratory [13]. In numerical simulation of cracked rock, Yang et al. [14] studied the strength, deformation, and crack evolution behavior of sandstone containing a single oval flaw under uniaxial compression by experiment and PFC. Zhao et al. [15] studied the mechanical behavior of rock containing two pre-existing holes by combining laboratory tests and PFC, and divided the deformation and failure process of rock mass containing hole defects into two stages: rock bridge penetration and overall instability. Liu et al. [16] and Zhou et al. [17] studied the failure modes of rock-like materials containing two circular holes, respectively. The crack development between two cavities and failure mechanism for different geometrical configurations were studied in detail using experimental and PFC. These studies were all based on rock materials with circular cavities, and the reason why the cracked rock mass is prone to failure has not been explained from a microscopic point of view. However, the cracks in natural rock mass are always narrow and long, and they can simplify as flat ellipses. Nowadays, the research on rocks with flat elliptical cracks is still insufficient, thus further research is urgently needed.

For this purpose, based on the PFC of the discrete element numerical simulation program, the numerical marble models were established with different ratios of long and short axes, and the crack propagation, strength variations under uniaxial compression were studied, and specially the numerical solutions in stress field concentration at the tip of elliptical crack were obtained. On the other hand, the analytical solutions of stress concentration factor at the tip of elliptical crack with different ratios of axes based on the theory of flat elliptical crack were obtained. The numerical solutions were verified by the analytical solutions to some extent. This research provided an effective direction for the cracked rock.

2 Numerical model of rock samples

2.1 Intact numerical model

Rock is a combination of mineral grains with a large number of joints, fissures, and hole defects, and is a typical heterogeneous medium [18]. So, the DEM is widely used in the field of rock mechanics. Particle flow code (PFC), based on discrete-element theory, is suitable for analyzing the deformation and failure mechanism of materials at the micro-scale [19,20].

PFC mainly describes the contact between particles with contact bond model and parallel bond model, which can simulate the compressive failure of rock materials along the normal or tangential direction and well reflect the failure mode of rock materials. Therefore, a parallel bonding model was used to establish numerical rock sample with the size of ϕ 50 mm × 100 mm based on the selection of bonding parameters. Tan et al. [21] showed that when the particle size ratio was 1.66, the value of particle radius has very little influence on the calculation results. Therefore, the particle size ratio was set to 1.66 and the minimum radius of particles was set to 0.3 mm. Based on the macro-mechanical parameters obtained from laboratory tests, the corresponding micro-mechanical property parameters shown in Table 1 were matched by trial-and-error method [22,23].

The stress–strain curves of uniaxial compression obtained in laboratory and numerical tests are shown in good consistency in Figure 1(a). More than that, the distribution of fracture cracks and even the failure surfaces shown in Figure 1(b) also demonstrate the numerical rock sample simulated closely to the natural marble. Furthermore, in Figure 1(b) red cracks represent microcracks caused by tensile and blue cracks represent

Table 1: Micro-mechanical parameters of numerical rock sample

Parameters	Values	Parameters	Values
Minimum particle size (mm)	0.3	Parallel bond modulus (GPa)	9.9
Particle size ratio	1.66	Parallel bond stiffness ratio	1.6
Density ($kg \cdot m^{-3}$)	2,700	Parallel bond normal strength (MPa)	29.4
Particle contact modulus (GPa)	9.9	Parallel bond tangential strength (MPa)	34
Particle contact stiffness ratio	1.6	Parallel bond internal friction angle (°)	50
Friction coefficient	0.5	Radius multiplier	1.0

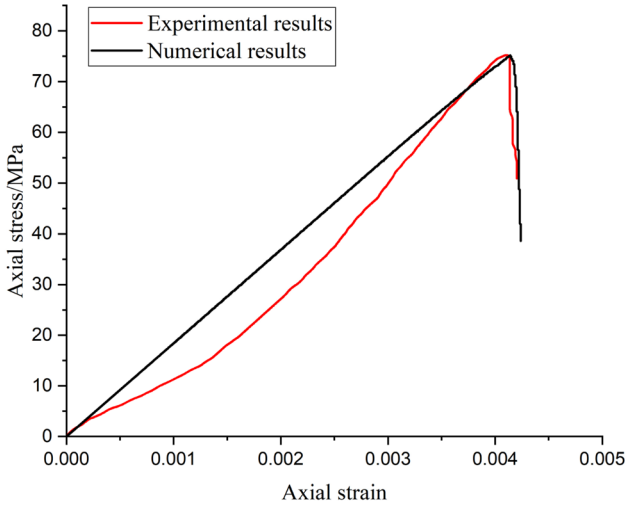

(a)

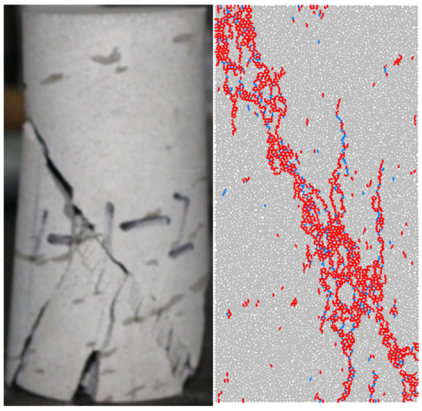

(b)

Figure 1: Stress–strain curves and damage surfaces of laboratory [24]: (a) stress–strain curve and (b) damage surfaces.

micro-cracks caused by shear. Two kinds of micro-cracks could be identified and counted automatically by PFC.

The mechanical properties obtained by natural marble and numerical model are shown in Table 2. The results demonstrated that the numerical rock sample established in this article had close physical and mechanical properties to the natural marble sample and can reflect the mechanical response of this marble under uniaxial compression.

Table 2: Mechanical parameters of marble and numerical model

Parameters	UCS	Elastic modulus	Poisson's ratio
Laboratory test	75.11 MPa	18.85 GPa	0.22
Simulation test	75.52 MPa	18.43 GPa	0.23
Error	0.5%	2.2%	4.5%

2.2 The numerical models with elliptical cracks

In order to study the influence of different ratios of long and short axes of prefabricated elliptical cracks on the mechanical properties and crack propagation laws of the marble, the length of b was 1 mm, the ratios of a:b were taken as 5, 7.5, 10, 12.5, and 15. In the other words, the long semi-axes were set to be 5, 7.5, 10, 12.5, and 15 mm, respectively. The micro-mechanical parameters followed Tables 1 and 2. A partial enlarged view of the prefabricated crack is shown in Figure 2, and a "measurement region" tangent to the elliptical crack was set at the end of the long axis of the elliptical crack which can measure the stress state of the particles in the region [25].

3 Propagation of cracks and their effects on strength

3.1 Effects of the propagation of micro-cracks

Figure 3 shows four key stages of the micro-crack propagation in numerical uniaxial compression processes of six numerical samples with elliptical cracks with different ratios of axes elliptical cracks. The four stages refer to the different stress states, 70% σ_c before the peak (σ_c is the peak strength), at the peak σ_c, 45% σ_c after the peak, and at the residual stage. These four stages can demonstrate the processes of micro-cracks initiated, propagated, and penetrated to form a macro-fracture surface finally. These

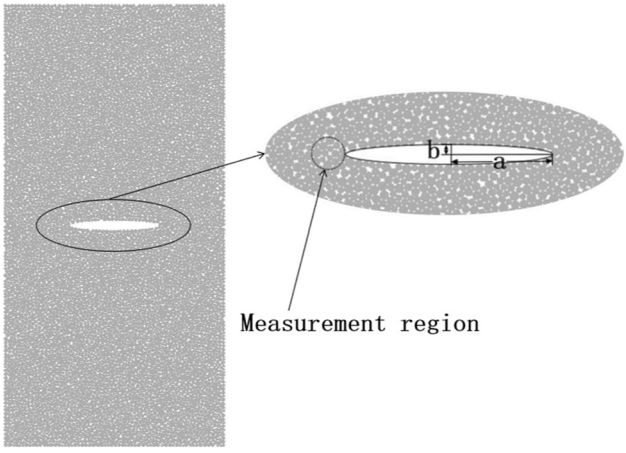

Figure 2: Partial enlarged view of prefabricated elliptical crack.

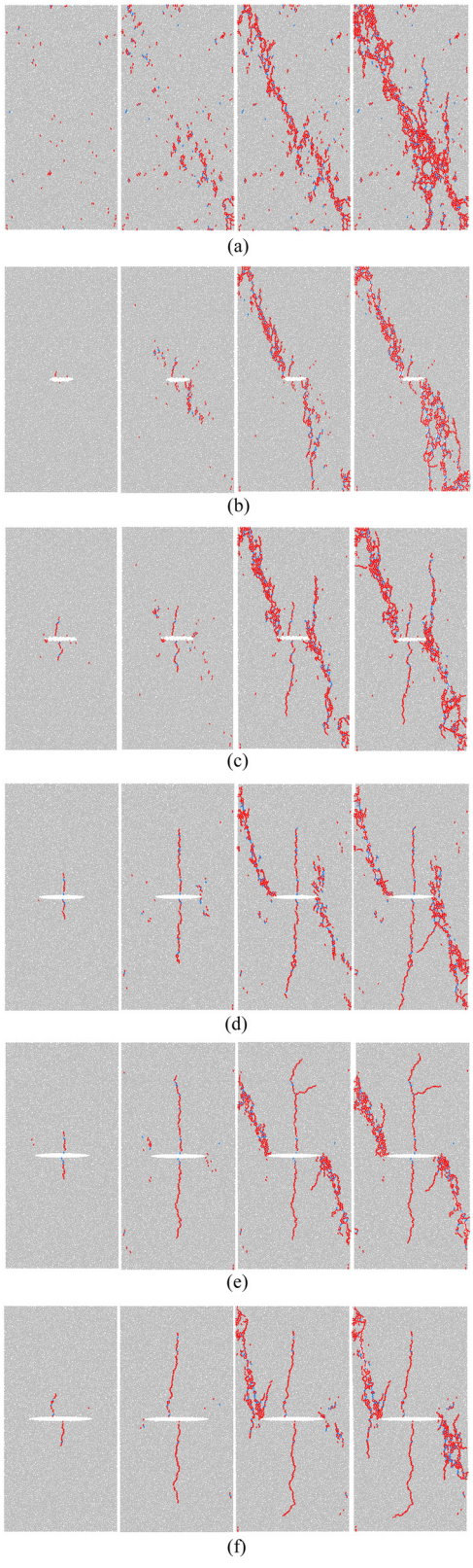

Figure 3: Micro-crack propagation of six numerical samples: (a) intact model, (b) a:b = 5, (c) a:b = 7.5, (d) a:b = 10, (e) a:b = 12.5, and (f) a:b = 15.

results were realized by the command stream written to save the states in numerical test every 1,000 time steps with FISH language in PFC.

Shown in Figure 3(a), for intact numerical rock sample, the tensile micro-cracks appeared radically at 70% σ_c before peak stress. As tensile micro-cracks increased various shear micro-cracks decreased at the peak stress. At 45% σ_c after the peak, the tensile micro-cracks increased sharply and penetrated, forming an obvious failure surface, and the shear micro-cracks were mainly distributed near the damage surface.

For numerical rock samples with elliptical cracks, tensile micro-cracks, a small amount of shear micro-cracks initiated near both ends of the short axis of the elliptical crack. At the peak stress, the initial crack gradually extended, and the tensile micro-cracks also appeared in different degrees at both ends of the long axis of the ellipse, forming wing cracks, the shear micro-cracks spread near the fracture. At 45% σ_c after the peak, many secondary cracks generated along the direction of the wing cracks propagated, and the five models with elliptical cracks of rock had obvious fracture surfaces. With the increasing of the a:b of elliptical crack, the initial cracks expanded more fully to the upper and the lower surfaces of the model, and the secondary cracks near the wing cracks increased. During the failure procedures, tensile micro-cracks were the main cracks, shear micro-cracks were few in number.

In terms of macroscopic failure, the failure modes of models with elliptical cracks were similar. The initial cracks penetrated upward and downward from both ends of the short axis of the elliptical cracks, the wing cracks were generated at both the ends of the long axis, and the secondary cracks were near the wing cracks. The whole fracture processes were consistent with fracture behavior in the uniaxial compression test of 0° angle prefabricated elliptical crack samples in the laboratory [14,26,27].

3.2 Effects on strength

Figure 4 shows the stress–strain curves of the six numerical rock samples. Before the peak stress, the stress–strain curve of the intact numerical rock sample was relatively stable, while the five numerical rock samples with elliptical cracks showed different degrees of stress fluctuations, which were mainly caused by the initiation and propagation of micro-cracks. The numerical rock samples with elliptical cracks showed progressive deformation

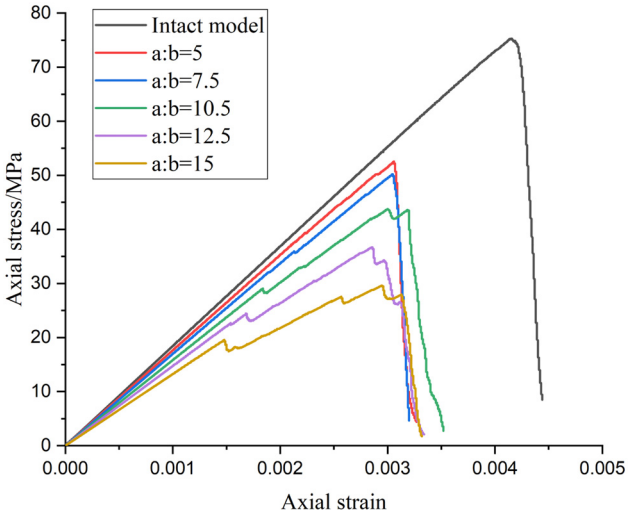

Figure 4: Stress–strain curves of six numerical models.

followed by brittle failure, and the linear elastic segment of the stress–strain curve of the numerical rock samples with elliptical cracks was significantly shortened. At the peak stress, the peak stress of the intact numerical rock sample was the highest. With the increase of the axial ratio a:b, the peak stress gradually decreased, and the reduction amplitude depended on the axial ratio of the elliptical crack. When a:b = 15, the strength was only 39.2% of the intact numerical rock sample. The existence of prefabricated cracks had a great influence on its strength.

Table 3 shows the changes of the uniaxial compressive strength, elastic modulus, and Poisson's ratio. With the increase of the ratios of a:b, the elastic modulus of the numerical rock samples gradually decreased while the Poisson's ratio increased. When a:b = 15, compared with the intact numerical rock sample, the elastic modulus decreased by 28%, and the Poisson's ratio increased by 121.7%. These were caused by the ratios of a:b of the prefabricated elliptical crack increased, the more the stress concentrated, the more aggressively the crack propagation. At the same time, when the deformations of the numerical rock samples increased gradually, the strength decreased gradually, and the strength gap between the intact numerical rock sample and the numerical rock samples with elliptical cracks became larger and larger. This was in agreement

Table 3: Physical parameters of six numerical models

Ratios of a:b	Intact	5	7.5	10	12.5	15
UCS (MPa)	75.52	52.61	50.21	43.63	36.39	29.53
Elastic modulus (GPa)	18.43	17.65	16.96	15.72	14.71	13.26
Poisson's ratio	0.23	0.27	0.32	0.39	0.46	0.49

with the experimental study on uniaxial compression of slab marble samples with prefabricated elliptical holes made by Zhu et al. [28], when the inclination angle of the elliptical holes was 0°. With the increase of the ratio of the long and short axes of the elliptical holes, the peak strength and elastic modulus of the models gradually decreased.

The crack initiation strength σ_{ci} is the axial stress at which the crack begins to occur when the specimen is subjected to uniaxial load. Potyondy and Cundall [29] defined that when the number of micro-cracks increases to a certain proportional coefficient (usually 1%) of the number of micro-cracks at the peak strength, the strength at this time is the crack initiation strength of the rock. The damage strength σ_{cd} corresponds to the unstable propagation stage of the micro-cracks, and the damage strength σ_{cd} of the models refers to the final failure surface formed. Table 4 lists the initiation strength, damage strength, number of micro-cracks at peak strength, as well as the determined initiation strength and damage strength of the six tests.

The existing research results have found that there is a certain proportional relationship between the crack initiation stress and its peak strength in uniaxial loading, and some scholars believe that the ratio is 0.3–0.5 [30,31], while others believe that the ratio is 0.7–0.8 [32]. Using different methods, the ratios founded by different scholars were quite different. In fact, this ratio has lots to do with cracks in the rock [33]. As shown in Table 4, the crack initiation strengths of the six groups of tests were distributed between 54 and 66% of their peak strengths, and gradually decreased with the increase of the ratios of axes of elliptical crack. The damage strength decreased with the increase of the a:b of elliptical crack, and the ratio of damage strength to peak strength also decreased gradually. Compared with the intact numerical rock sample, the crack initiation strength of crack decreased by 18.12% and the damage strength decreased by 28.23% when a:b = 15. Above all, the larger the proportion of prefabricated elliptical cracks in the numerical rock samples, the easier the numerical rock samples to be damaged, the earlier the micro-cracks appeared, the more serious the strength deterioration will be.

4 Analysis of stress field at the tip of cracks

4.1 Flat elliptical crack model

The stress field of the cracked rock mass changes under the action of the stress environment and the engineering load, and the stress concentration gradually occurs in the

Table 4: Characteristic strength of six models

Ratios of *a*:*b*	Number of micro-cracks at crack initiation strength	Crack initiation strength σ_{ci} (MPa)	Ratio of crack initiation strength to peak strength (%)	Number of micro-cracks at damage strength	Damage strength σ_{cd} (MPa)	Ratio of damage strength to peak strength (%)	Number of micro-cracks at peak strength	Peak strength (MPa)
Intact model	3	49.63	65.72	37	63.14	83.61	276	75.52
5	2	34.16	64.93	22	44.72	85.16	173	52.61
7.5	1	29.46	58.67	15	35.74	71.45	129	50.21
10	3	24.92	57.12	51	28.35	64.98	346	43.63
12.5	2	20.26	55.22	38	24.31	66.26	196	36.69
15	3	16.05	54.35	82	17.72	60.01	286	29.53

crack end region. When the stress concentration reaches a certain level, it will cause localized deformation processes such as initiation, evolution, and overlap of internal cracks, and gradually deteriorate the mechanical properties of rock mass, resulting in unstable rock mass destruction [34]. Jiang et al. [35] also pointed out that the development process of cracked rock is the result of stress concentration and continuous release of concentrated stress to surrounding elements. Griffith first simplified the crack to an ellipse, and it is still used as a classical theory. As shown in Figure 5, the long and short axes of the elliptical crack are 2a and 2b, respectively, the angle between the long axis and the axial pressure q is α. Aiming at the flat elliptical crack, the crack initiation position of the prefabricated elliptical crack model under uniaxial compression and the analytical solution expression of the tangential stress at the hole edge were analyzed.

Using the conformal transformation method, the plane z outside the elliptical crack is mapped to the inside of the unit circle on the plane ζ, as shown in Figure 6, where ρ is the radius of the mapping plane.

Using the complex variable function, the conformal mapping is obtained:

$$z = \omega(\zeta) = R(1/\zeta + m\zeta), \tag{1}$$

In formula (1), $\xi = \rho \exp(i\theta)$, $R = (a + b)/2$, $m = (a - b)/(a + b)$, R and m are real numbers, and $R > 0$, $0 \le m \le 1$.

On the plane ζ, θ turns counterclockwise, and the maximum point corresponding to the tangential stress

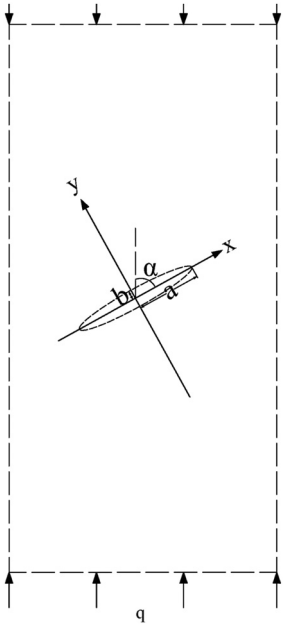

Figure 5: Mechanical model of flat elliptical crack.

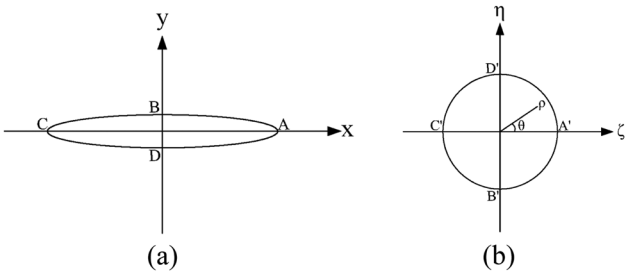

Figure 6: Diagram of plane projection: (a) plane z and (b) plane ζ.

σ_θ on the mapping circle is θ_0. According to the linear elasticity theory, the maximum values of tangential stress θ_0 meet following condition [36]:

$$\begin{aligned}&(1-m^2)(\cos 2\alpha - m)\sin 2\theta_0\\&\quad + [(1-m^2)\cos 2\theta_0 - 2m]\ \sin 2\alpha = 0.\end{aligned} \tag{2}$$

Since the conformal mapping is a one-to-one correspondence, the maximum point θ_p of the tangential stress on the edge of the elliptical crack can be determined: $\tan\theta_p = -\frac{b}{a}\tan\theta_0$, so the cracking point of the elliptical crack can be obtained as:

$$\begin{aligned}x_p &= R(1+m)\cos\theta_p\\ y_p &= -R(1-m)\sin\theta_p.\end{aligned} \tag{3}$$

The analytical solution of the tangential stress around the elliptical hole can be calculated as follows:

$$\sigma_\theta = q\left[\frac{1-m^2+2m\cos 2\alpha - 2\cos(2\theta+2\alpha)}{1+m^2-2m\cos 2\theta}\right]. \tag{4}$$

In particular, when the load is perpendicular to the long axis of the ellipse, it is the uniaxial compression test of marble with the prefabricated elliptical crack discussed in this article. Substituting $\alpha = 90°$ into formulas (2) and (4), respectively:

$$(1-m^2)(-1-m)\sin 2\theta_0 = 0, \tag{5}$$

$$\sigma_\theta = q\left[\frac{1-m^2-2m+2\cos 2\theta}{1+m^2-2m\cos 2\theta}\right]. \tag{6}$$

Substituting the values of different axial ratios in this article into formula (3), respectively, the crack initiation position of the numerical rock samples can be obtained as:

$$\begin{aligned}&\theta_0 = 0 \text{ or } \pi,\ \theta_p = 0 \qquad x_p = \pm a,\ y_p = 0\\ &\theta_0 = \pm\frac{\pi}{2},\ \theta_p = \pm\frac{\pi}{2} \ \Rightarrow\ x_p = 0,\ y_p = \pm b.\end{aligned} \tag{7}$$

Calculate the first derivative of θ in formula (6), and take $d\sigma_\theta/d\theta = 0$:

$$\sin 2\theta(m^3+m^2-m-1) = 0. \tag{8}$$

In formula (8), $f(m) = m^3 + m^2 - m - 1 < 0$ is always established when the values of m are in the interval $[0, 1]$. Accordingly, the tangential stress around the elliptical hole is obtained as [37]:

$$\begin{aligned}(\sigma_\theta)_{\max} &= \sigma_\theta|_{\theta=0,\pi} = q\frac{3+m}{1-m}\\ (\sigma_\theta)_{\min} &= \sigma_\theta|_{\theta=\pm\frac{\pi}{2}} = -q.\end{aligned} \tag{9}$$

Formula (9) shows that for the horizontally placed elliptical cracks, the maximum tangential stress appears at the endpoint of the short axis, which reasonably explains the test phenomenon of vertical tensile cracks in Figure 4 under the action of compression load. Moreover, the stress concentration of short axis end is unrelated to m values, while the stress concentration of long axis end is extremely sensitive to m values (the more closely m approaches to 1, the more significant the stress concentration is). The stress concentration factor of analytical solution is defined as k, which reflects the severity of the stress concentration phenomenon at the crack tip. The values of the stress concentration factor k are as follows:

$$k = \frac{\sigma_\theta}{q} = \frac{3+m}{1-m}. \tag{10}$$

In formula (10), σ_θ is the tangential stress at the end point of the long axis of the elliptical crack, q is the axial pressure of the numerical rock samples, and $m = (a-b)/(a+b)$.

Substituting the different axial ratios in this article into Equation (10), the stress concentration factors k of the analytical solutions at the end of the long axis in the five tests with elliptical cracks are obtained as shown in Table 5.

4.2 Stress field analysis in PFC

The method of using the numerical solutions obtained by numerical simulation to check the analytical solutions obtained by theoretical analysis has been adopted by many scholars and certain research results were obtained [38–40]. In PFC, the contacts between particles of marble can be represented as lines with color difference, which

Table 5: k of analytical solutions of five cracked models

Ratios of a:b of elliptical crack	5	7.5	10	12.5	15
k of analytical solutions	11	16	21	26	31

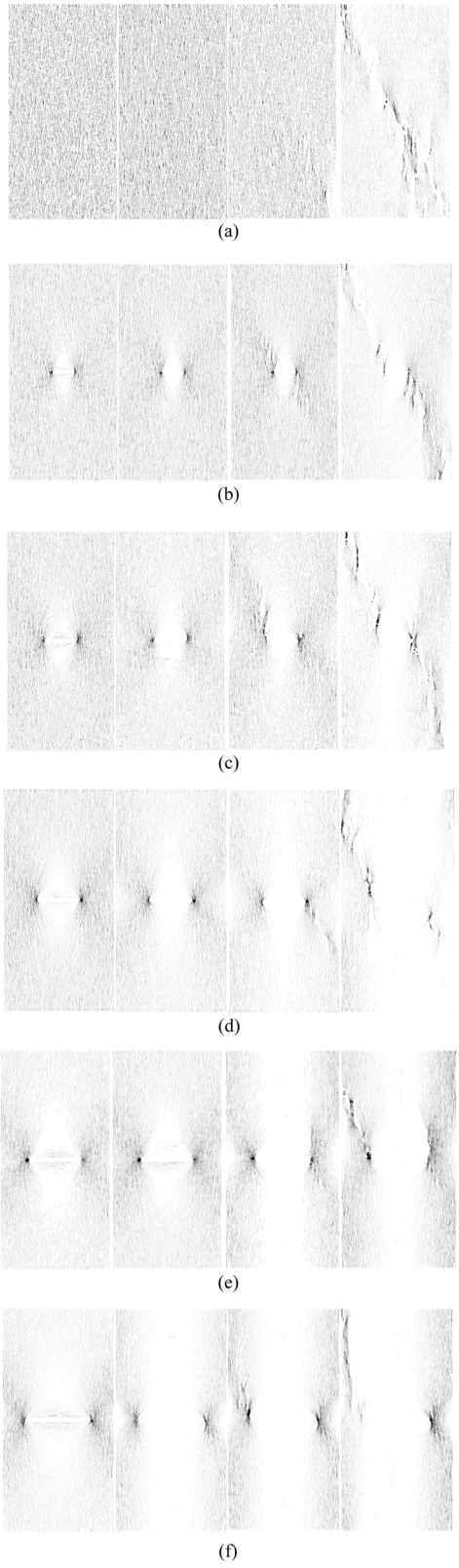

Figure 7: The force chains change of six models: (a) intact model, (b) a:b = 5, (c) a:b = 7.5, (d) a:b = 10, (e) a:b = 12.5, and (f) a:b = 15.

indicate the size of contact force between the particles, thus forming diagrams of force chains. As shown in Figure 7, four monitoring points were set: the σ_{ci} of initiation strength, the σ_{cd} of damage strength, the σ_c of peak strength, and 45% σ_c after the peak, in order to observe the changes of the contact forces between the particles through the diagrams of force chains.

In order to study the stress field concentration at the end of the long axis of the crack, the tip of elliptical crack was monitored for stress using the "measurement region" of PFC (Figure 2). The stress measured by the "measurement region" is the average value of the particles in the circle, and the stress state in the four directions of xx, yy, xy, and yx in the overall x–y coordinate system can be output. Pu et al. [37] believed that although the σ_{xx} of normal stress at the tip of the elliptical crack contributed to the stress concentration at the tip, the σ_{yy} of tangential stress contributed more to the stress concentration at the tip, the normal stress at the crack tip can be ignored for the development of micro-cracks at the tip when the crack inclination angle is small. The k as the stress concentration factor of the numerical solution obtained is as follows:

$$k = \frac{\sigma_{yy}}{q}. \tag{11}$$

In formula (11), σ_{yy} is the stress in the yy direction at the left end of the long axis of the elliptical crack when the peak stress was loaded and q is the axial pressure of the models of marble.

k of numerical solutions of stress concentration factor of the five cracked models were counted. As the ratios of a:b of the elliptical crack increased, the values of k increased, as shown in Table 6.

In order to contrast the trend of k obtained from the analytical solution and the numerical solution more clearly and intuitively, the diagram of two sets of k was drawn as shown in Figure 8.

The stress concentration factor k of analytical solution obtained using linear elasticity theory was higher than that obtained using PFC. The trends of the two groups of k values were highly consistent, and the analytical solution also showed a linear relationship approximately. More than this, the slopes of the two groups were

Table 6: k of numerical solution of five cracked models

Ratios of a:b of elliptical crack	5	7.5	10	12.5	15
k of numerical solutions	7.1	11.4	16.5	21.3	26.4

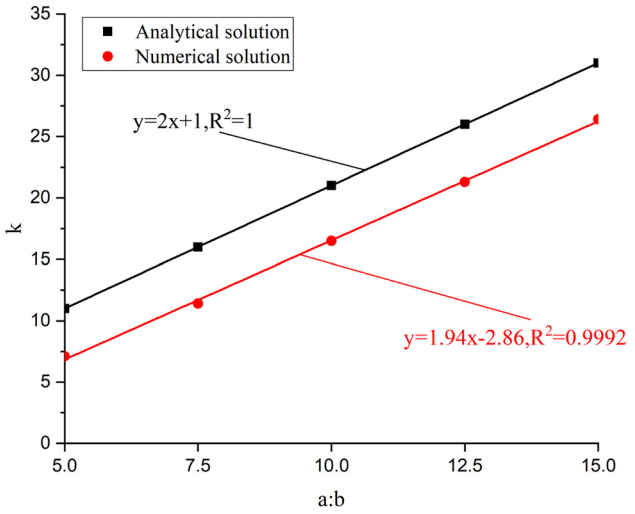

Figure 8: The *k*-value of analytical solutions and numerical solutions.

almost same, showing an approximately parallel relationship. For rock material the reasons for this difference may be as follows: the analytical solutions are based on elastic theory and continuum mechanics, and the numerical solutions are based on DEM. The basic theoretical framework of the two is different, which leads to this diversity.

The above analysis process interpreted the influences of prefabricated elliptical cracks on the microscopic stress field and macroscopic strength of the marble models, and the comparison of the analytical and numerical solutions of stress concentration factor *k* showed that the stress concentration is an important reason for failure of rock mass with elliptical cracks. This will provide a new direction of simulation for materials that are laborious to test in the laboratory.

5 Conclusions

The stress concentration is an important reason for failure of rock mass with elliptical cracks. The crack tip should be paid more attention in natural rock mass.

(1) When the models of marble with prefabricated elliptical crack were destroyed, the initial cracks occurred and extended at the end of the short axis of the crack, and the wing cracks occurred at both ends of the long axis, gradually forming macro-cracks, while the secondary cracks extended near the wing cracks.

(2) With the increase of the *a*:*b* of the long and short axes of the elliptical crack,the peak strength gradually decreased, the elastic modulus gradually decreased, Poisson's ratio gradually increased, and the total number of micro-cracks decreased, the crack initiation strength and damage strength also decreased gradually.

(3) Elliptical cracks with different axial ratios had a significant impact on the stress field at the tip. The greater the axial ratio, the more severe the stress concentration at the tip. The analytical solutions of the stress concentration factor *k* were obtained from the flat elliptic model, which were highly consistent with the numerical solutions of the stress concentration factor measured by PFC. This will be an effective way to design and simulate complicated test which was hard to carry in laboratory for studying the micro-failure mechanism and macro-fracture process of the material.

Acknowledgments: The authors would like to thank the National Natural Science Foundation of China (Nos. 51609080 and 51708188) and the Hubei Key Research and Development projects (No. 021BAA050). We also would like to express our sincere gratitude to the editor and reviewers for their valuable comments, which have greatly improved this article.

Funding information: The National Natural Science Foundation of China (Nos. 51609080 and 51708188) and the Hubei Key Research and Development projects (No. 021BAA050).

Author contributions: Yang: conceptualization and methodology; Cheng, Yin, and Hou: validation and investigation; Zhang: supervision.

Conflict of interest: Authors state no conflict of interest.

Data availability statement: This data that supports the findings of this study are available from the corresponding author upon the reasonable request.

References

[1] Wang, Y., J. Tang, Z. Dai, and T. Yi. Experimental study on mechanical properties and failure modes of low-strength rock samples containing different fissures under uniaxial compression. *Engineering Fracture Mechanics*, Vol. 197, 2018, pp. 1–20.

[2] Wu, T. H., Y. Zhou, L. Wang, J. H. Sun, H. Zhao, and Z. Sun. Mesoscopic study of interaction mechanism between circular hole and fissures in rock under uniaxial compression. *Rock and Soil Mechanics*, Vol. 39, No. S2, 2018, pp. 463–272.

[3] Li, C. J., X. B. Li, and D. Y. Li. Particle flow analysis of fracture characteristics of marble with a single hole. *Chinese Journal of Engineering*, Vol. 3912, 2017, pp. 1791–1801.
[4] Chen, X., X. Peng, D. W. Li, and W. T. Lv. Analysis on cracking mechanism fractured rock mass under uniaxial compression based on the two fracture criteria. *Engineering Mechanics*, Vol. 30, No. 10, 2013, pp. 227–235.
[5] Inglis, C. E. Stresses in a plate due to the presence of crack or sharp corner. *Engineering*, Vol. 95, 1913, p. id. 415.
[6] Griffith, A. A. The phenomena of rupture and flow in solids. *Philosophical Transactions of the Royal Society. of London*, Vol. A221, 1921, pp. 163–198.
[7] Arianfar, A., A. Ramezanzadeh, and M. Khalili. Numerical modeling of closure effect of natural fracture surfaces of rock on behavior of fluid flow. *Bulletin of Engineering Geology and the Environment*, Vol. 80, No. 3, 2021, pp. 2335–2348.
[8] Vahab, S. and H. Haeri. Three-dimensional numerical modeling of effect of bedding layer on the tensile failure behavior in hollow disc models using Particle Flow Code (PFC3D). *Structural Engineering & Mechanics*, Vol. 68, No. 5, 2018, pp. 537–547.
[9] Sarfarazi, V., H. Haeri, A. B. Shemirani, and Z. Zhu. Shear behavior of non-persistent joint under high normal load. *Strength of Materials*, Vol. 49, No. 2, 2017, pp. 320–334.
[10] Wang, H., H. Zhou, S. C. Shang, and C. Jiang. Development and application of rock fracture propagation numerical simulation system. *Geotechnical and Geological Engineering*, Vol. 40, No. 6, 2022, pp. 3075–3090.
[11] Wang, P. F., C. H. Li, and W. H. Tan. Numerical simulation of fracture failure characteristics of rock mass with multiple parallel fractures under seepage stress coupling. *Arabian Journal of Geosciences*, Vol. 15, No. 7, 2022, pp. 1–11.
[12] Duan, K., C. Y. Kwok, and X. Ma. DEM simulations of sandstone under true triaxial compressive tests. *Acta Geotechnical*, Vol. 12, No. 3, 2017, pp. 495–510.
[13] Zhao, W. H., R. Q. Huang, and M. Yan. Mechanical and fracture behavior of rock mass with parallel concentrated joints with different dip angle and number based on PFC simulation. *Geomechanics and Engineering*, Vol. 8, No. 6, 2022, pp. 757–767.
[14] Yang, S. Q., W. L. Tian, Y. H. Huang, Z. G. Ma, L. F. Fan, and Z. J. Wu. Experimental and discrete element modeling on cracking behavior of sandstone containing a single oval flaw under uniaxial compression. *Engineering Fracture Mechanics*, Vol. 194, 2018, pp. 154–174.
[15] Zhao, Z. L., H. W. Jing, X. S. Shi, and G. S. Han. Experimental and numerical study on mechanical and fracture behavior of rock-like specimens containing pre-existing holes flaws. *European Journal of Environmental and Civil Engineering*, Vol. 26, No. 1, 2022, pp. 299–319.
[16] Liu, B., Y. Zhou, Y. T. Gao, and C. S. Xu. Experimental and numerical study on crack development characteristics between two cavities in rock-like material under uniaxial compression. *Theoretical and Applied Fracture Mechanics*, Vol. 109, 2020, id. 102755.
[17] Zhou, Y., B. Liu, L. Wang, X. Li, and Y. P. Ding. Mesoscopic mechanical properties of rock-like material containing two circular holes under uniaxial compression. *Chinese Journal of Rock Mechanics and Engineering*, Vol. 36, No. 11, 2017, pp. 2662–2671.
[18] Zhu, Q. Q., D. Y. Li, Z. Y. Han, X. B. Li, and Y. L. Zhou. Mechanical properties and fracture evolution of sandstone specimens containing different inclusions under uniaxial compression. *International Journal of Rock Mechanics & Mining Sciences*, Vol. 115, 2019, pp. 33–47.
[19] Haeri, H., V. Sarfarazi, and A. B. Shenmirani. Experimental and numerical study of shear crack propagation in concrete specimens. *Computers and Concrete*, Vol. 20, No. 1, 2017, pp. 57–63.
[20] Haeri, H., V. Sarfarazi, and Z. M. Zhu. Effect of normal load on the crack propagation from pre-existing joints using Particle Flow Code (PFC). *Computers and Concrete*, Vol. 19, No. 1, 2017, pp. 99–110.
[21] Tan, P., Q. H. Rao, Z. Li, Q. Zhang, and W. Yi. A new method for PFC3D fine parameter calibration considering fracture toughness. *Journal of Central South University* (*Science and Technology*), Vol. 52, No. 8, 2021, pp. 2849–2866.
[22] Huang, Y. H., S. Q. Yang, and J. Zhao. Three-dimensional numerical simulation on triaxial failure mechanical behavior of rock-like specimen containing two unparallel fissures. *Rock Mechanics & Rock Engineering*, Vol. 49, No. 12, 2016, pp. 1–19.
[23] Fan, X. and P. Cao. Numerical analysis of mechanical behavior of specimens with two cracks under uniaxial compression based on PFC3D. *Journal of Central South University: Natural Science Edition*, Vol. 46, No. 7, 2015, pp. 2635–2642.
[24] Yang, Y. S., H. Zhou, C. Q. Zhang, K. Zhang, and F. Yan. Experimental investigation on time-lag failure properties of marble under uniaxial compressive test. *Rock and Soil Mechanics*, Vol. 32, No. 9, 2011, pp. 2714–2270.
[25] Itasca Consulting Group. *PFC 5.0 Documentation, User's Guide*. Itasca Consulting Group, Inc., Minneapolis, MN, USA, 2018.
[26] Huang, Y. H., S. Q. Yang, M. R. Hall, W. L. Tian, and P. F. Yin. Experimental study on uniaxial mechanical properties and crack propagation in sandstone containing a single oval cavity. *Archives of Civil and Mechanical Engineering*, Vol. 18, No. 4, 2018, pp. 1359–1373.
[27] Yao, L. Experimental study on the mechanical properties of marble with elliptical hole defects and particle flow simulation. *Master's thesis*, China University of Mining and Technology, Jiangsu, 2019.
[28] Zhu, Q. Q., D. Y. Li, and X. B. Li. Experimental study on deformation and failure mechanical properties of marble with prefabricated elliptical holes. *Chinese Journal of Rock Mechanics and Engineering*, Vol. 38, No. S1, 2019, pp. 2724–2733.
[29] Potyondy, D. O. and P. A. Cundall. A bonded-particle model for rock. *International Journal of Rock Mechanics and Mining Sciences*, Vol. 41, No. 8, 2004, pp. 1329–1364.
[30] Fan, X., P. H. S. W. Kulatilake, X. Chen, and P. Cao. Crack initiation stress and strain of jointed rock containing multi-cracks under uniaxial compressive loading: a particle flow code approach. *Journal of Central South University*, Vol. 22, No. 2, 2015, pp. 639–645.
[31] Holcomb, D. J., and L. S. Costin. *Damage in brittle materials: experimental methods*, Geomechanics Division, Sandia National Labs, Albuquerque, NM, USA, 1986, pp. 1–50.
[32] Martin, C. D. and N. A. Chandler. The progressive fracture of Lac du Bonnet granite. *International Journal of Rock Mechanics and Mining Sciences & Geomechanics Abstracts*, Vol. 31, No. 6, 1994, pp. 643–659.

[33] Yin, D. W., S. J. Chen, X. Q. Liu, G. Wang, H. F. Ma, and B. T. Shen. Simulation of regular particle flow on granite fracture stress and damage stress. *Journal of Applied Basic and Engineering Science*, Vol. 264, No. 4, pp. 808–820.

[34] Lv, X. B., Q. H. Zhao, and G. Han. Failure process of rock with single precast crack based on ratio of concentration stress to peak stress. *Rock and Soil Mechanics*, Vol. 38, No. S1, 2017, pp. 87–95.

[35] Jiang, M. J., N. Zhang, Z. F. Shen, and H. Chen. Discrete element analysis of crack propagation mechanism in cracked rock mass under uniaxial compression. *Rock and Soil Mechanics*, Vol. 35, No. 11, 2015, pp. 3293–3300.

[36] Zhang, D. F., W. S. Zhu, S. C. Li, and Y. S. Guo. Effects of confining pressure and crack water pressure on initial cracking of elliptical cracks in rock. *Chinese Journal of Rock Mechanics and Engineering*, No. Z2, 2004, pp. 4721–4725.

[37] Pu, C. Z., S. J. Yang, and C. Y. Zhang. Discussion on fracture mechanism of fracture body affected by opening degree. *Chinese Journal of Geotechnical Engineering*, Vol. 41, No. 10, 2019, pp. 1836–1844.

[38] Yang, Y. S., C. Wei, Z. R. Zhang, H. Y. Tian, K. Y. Li, and C. P. Huang. Energy evolution law of marble failure process under different confining pressures based on particle discrete element method. *Frontiers in Materials*, Vol. 8, 2021, pp. 1–8.

[39] Wang, H. P., T. Song, J. W. Yan, P. Xiang, S. Y. Feng, and D. Hui. Improved analytical method for interfacial-slip control design of steel-concrete composite structures. *Symmetry*, Vol. 13, No. 7, 2021, p. id. 1225.

[40] Zhang, X. L., A. Z. Lv, and S. J. Wang. Stress analytical solution for orthotropic non-circular hydraulic tunnels. *Chinese Journal of Rock Mechanics and Engineering*, Vol. 36, No. S2, 2017, pp. 3808–3815.